Spring Arctic Atmospheric Preconditioning: Do Not Rule Out Shortwave Radiation Just Yet

Joseph Sedlar

Department of Meteorology, Stockholm University, Stockholm, Sweden, and Cooperative Institute for Research in Environmental Sciences, University of Colorado Boulder, Boulder, Colorado

(Manuscript received 20 October 2017, in final form 6 March 2018)

ABSTRACT

Springtime atmospheric preconditioning of Arctic sea ice for enhanced or buffered sea ice melt during the subsequent melt year has received considerable research focus. Studies have identified enhanced poleward atmospheric transport of moisture and heat during spring, leading to increased emission of longwave radiation to the surface. Simultaneously, these studies ruled out the role of shortwave radiation as an effective preconditioning mechanism because of relatively weak incident solar radiation, high surface albedo from sea ice and snow, and increased clouds during spring. These conclusions are derived primarily from atmospheric reanalysis, which may not always accurately represent the Arctic climate system. Here, top-of-atmosphere shortwave radiation observations from a state-of-the-art satellite sensor are compared with ERA-Interim reanalysis to examine similarities and differences in the springtime absorbed shortwave radiation (ASR) over the Arctic Ocean. Distinct biases in regional location and absolute magnitude of ASR anomalies are found between satellite-based measurements and reanalysis. Observations indicate separability between ASR anomalies in spring corresponding to anomalously low and high ice extents in September; the reanalysis fails to capture the full extent of this separability. The causes for the difference in ASR anomalies between observations and reanalysis are considered in terms of the variability in surface albedo and cloud presence. Additionally, biases in reanalysis cloud water during spring are presented and are considered for their impact on overestimating spring downwelling longwave anomalies. Taken together, shortwave radiation should not be overlooked as a contributing mechanism to springtime Arctic atmospheric preconditioning.

1. Introduction

As the Arctic climate undergoes rapid changes, it is crucial to improve the process-level understanding regarding the mechanisms and feedbacks that favor the observed changes. Sea ice extent and volume have shown a nearly continuous negative trend since satellite records began (e.g., Kwok and Rothrock 2009; Kwok et al. 2009; Comiso 2012; Cavalieri and Parkinson 2012; Parkinson and DiGirolamo 2016). The reduction of reflective and insulating sea ice and overlying snow cover is trending toward a larger fraction of darker (less reflective) and relatively warmer open ocean surfaces more susceptible to absorbing shortwave radiation (Kashiwase et al. 2017). The abundance of multiyear sea ice is being replaced by thinner first year ice more prone to earlier melt at the onset of the sea ice melt season (e.g., Serreze and Stroeve 2015; Mortin et al. 2016). Anomalies in atmospheric circulation are impacting the heat and moisture content that is transported poleward over the thinning sea ice (e.g., Graversen et al. 2011; Serreze and Stroeve 2015; Sedlar and Tjernström 2017). Subsequently, radiative and turbulent fluxes over the ice become altered, and a number of feedback mechanisms at the surface and within the atmosphere can further contribute to the observed amplified Arctic warming (e.g., Pithan and Mauritsen 2014).

Atmospheric preconditioning over the Arctic examines and quantifies the impact of processes in the atmosphere during winter, spring, and early summer that effectively modulate the extent of melt for snow and sea ice. Strictly considering the atmosphere, these processes include anomalies in the convergence of heat and moisture, alterations to the lower-tropospheric static stability and subsequent dynamic surface heat fluxes, and changes in the distribution and radiative impact of

cloud cover. To quantify these individual and interrelated contributions, Kapsch et al. (2013) identified years with anomalously low sea ice extent (SIE) in September, called low ice years (LIYs), when Arctic sea ice reaches its minimum. For these years, atmospheric, radiative, and turbulent components are detrended and their anomalies during the spring months preceding this September LIY anomaly are composited and contrasted with those when the September SIE is anomalously high [high ice years (HIYs)]. Identifying September LIY and HIY anomalies is achieved by calculating standardized anomalies of SIE, essentially detrending the SIE data record and identifying years when it surpasses a standardized anomaly threshold, here larger than ±0.5. Figure 1a highlights the interannual variability of the September SIE standardized anomaly time series from monthly passive microwave imager measurements of SIE generated by the NASA Team algorithm (e.g., Cavalieri et al. 1996).

In general, the extent of sea ice during spring is not a meaningful predictor of the subsequent ice extent come September (Petty et al. 2017). For example, in Figs. 1b–g, SIE standardized anomalies for March through August are calculated and plotted against their subsequent September SIE standardized anomalies for HIYs (blue) and LIYs (red) over the period 1979–2016. Considerable variability is evident, as both LIY and HIY anomalies fluctuate monthly between anomalously low and high ice extents, even though their September values classify these years as robust anomalies. Correlation coefficients during March through May highlight this variability and indicate that the monthly SIE anomaly and that of September are often weakly anticorrelated. It is not until June or July that the monthly anomalies in SIE begin to align with their September classification of either HIY or LIY. Based on these later correlation alignments, the focus of this study will be on the spring and early summer months spanning from March through June.

Following the results of Kapsch et al. (2013), several studies have analyzed the winter and spring months in an effort to characterize important anomalies in the atmosphere that may be responsible for preconditioning and contributing to anomalies in September Arctic SIE. An emerging consensus from these studies is that LIYs tend to experience positive flux anomalies of surface downwelling longwave (LWD) radiation during spring, while downwelling shortwave (SWD) radiation anomalies were negative (Kapsch et al. 2013, 2014; Cox et al. 2016; Mortin et al. 2016). Liu and Key (2014) and Cao et al. (2017) extended the seasonal analysis to winter months and found that anomalous LWD fluxes were effective in preconditioning the sea ice already in winter

(SWD is absent during the polar winter). Observational studies on the Arctic ice pack have shown that longwave fluxes are critical in modifying the surface energy budget, the surface skin temperature, and the heat transfer through the snow and sea ice pack; these are closely connected to the structure and microphysical properties of overlying clouds (Shupe and Intrieri 2004; Sedlar et al. 2011; Persson 2012). Sedlar et al. (2011) demonstrated that enhanced LWD from supercooled liquid-bearing clouds also has the potential to alter the lower-tropospheric stability structure, which in turn can impact the direction and magnitude of near-surface turbulent fluxes. Thus, longwave radiation, through its important impact on the surface energy budget, is a physically plausible mechanism contributing to winter and spring sea ice preconditioning.

The role of shortwave radiation anomalies as a mechanism contributing to spring and early summer preconditioning has also been examined. Kapsch et al. (2013, 2016) and Mortin et al. (2016) correlated negative SWD anomalies during spring with higher ice extent and later melt season onset. However, Choi et al. (2014), using satellite observations of absorbed shortwave radiation (ASR), found that anomalies in shortwave radiation already during May were significantly correlated with the seasonal SIE minimum; covariance lead–lag analysis between absorbed shortwave radiation and SIE pointed toward the importance of shortwave anomalies in late spring and early summer as an intricate driver of the seasonal sea ice melt evolution. Cox et al. (2016) argue that both longwave and shortwave preconditioning of sea ice may work in unison, concluding that anomalies in surface radiation are instead a matter of timing. Correspondingly, a modeling study by Schröder et al. (2014) found a strong negative correlation between the fraction of melt pond occurrence in late spring and the SIE in September; this suggests a decreased surface albedo and increased shortwave absorption may contribute to an enhanced ice-albedo feedback. Kashiwase et al. (2017) described a situation where increased divergence of sea ice in areas commonly covered by landfast ice can result in increased open water fraction and enhanced shortwave radiation absorption by the less reflective open water areas.

Conclusions drawn regarding Arctic spring preconditioning mechanisms generally rely on atmospheric reanalysis datasets, or a blend of spaceborne observational datasets and reanalysis. Therefore these studies pivot on the accurate representation of atmospheric, radiative, and turbulent processes in reanalysis and global climate model (GCM) simulations. Many of these processes in reanalysis and GCMs are known to contain biases over the high-latitude Arctic, where observational
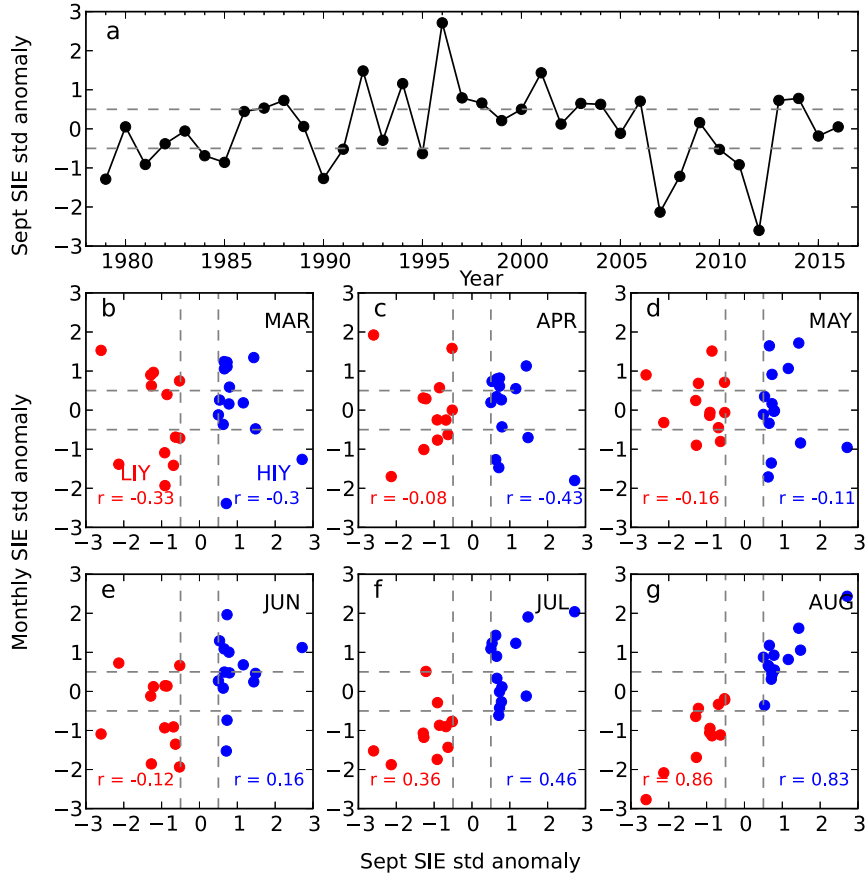
FIG. 1. (a) September SIE standardized anomalies computed for 1979–2016. (b)–(g) Monthly (March through August) SIE standardized anomalies plotted against the corresponding September SIE standardized anomalies for the 12 yr designated as (red) LIYs and 14 yr designated as (blue) HIYs (years where September SIE standardized anomaly is $>\pm 0.5$ standardized value: gray dashed lines in panel Fig. 1a). Correlation coefficient values between the monthly and September SIE standardized anomalies are presented in each panel.

constraints of physical processes are sparse, particularly in the representation and distribution of surface albedo, cloud fraction, cloud phase, cloud-radiative interactions, near-surface turbulent heat fluxes, and lower-tropospheric thermodynamic structure (Tjernström et al. 2008; Karlsson and Svensson 2013; de Boer et al. 2014; Wesslén et al. 2014; Sotiropoulou et al. 2016).

In this study, the focus turns to state-of-the-art satellite observations at the top of the atmosphere (TOA) measuring the amount of shortwave radiative energy absorbed within the climate system over the Arctic Ocean from 2000 to 2016. Following Choi et al. (2014), the purpose is to quantify the observed relationship between ASR and physical processes that critically impact ASR from March through June (early spring to early summer). Simultaneously, these observed relationships are compared with ERA-Interim reanalysis through a comparison of ASR and variables impacting

ASR for LIYs with HIYs during the observation records from 2000 to 2016. Because ERA-Interim is frequently used for Arctic studies, it is analyzed in unison to understand the robustness in sea ice atmospheric preconditioning results from studies that have applied ERA-Interim fields.

2. Data and methodology

a. Observations and reanalysis

This study centrally focuses on ASR at the TOA for one straightforward reason: this variable is accurately observed from space, and does not rely on a priori assumptions and radiative transfer models to estimate it. Observations of ASR during spring and early summer (March through June) over the years 2000 to 2016 are analyzed from CERES (Clouds and the Earth's Radiant Energy System). CERES directly observes incident
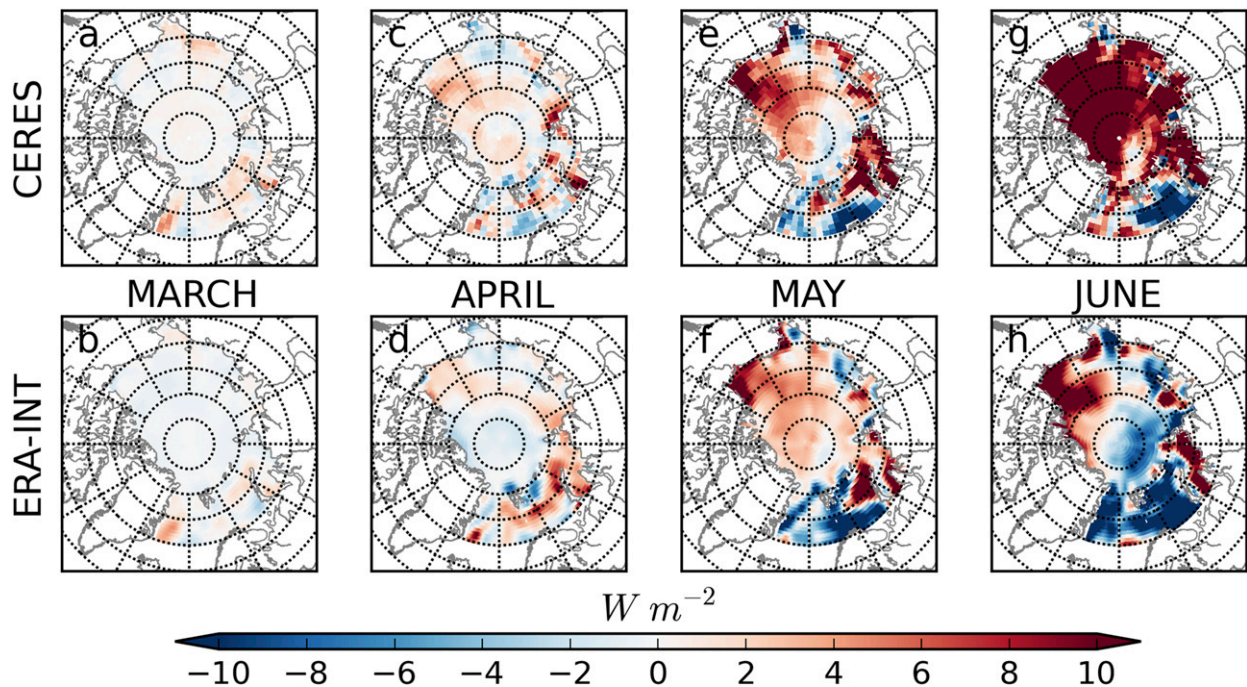
FIG. 2. Spring and early summer monthly spatial detrended anomalies in ASR for LIYs − HIYs (W m^{-2}), showing (top) CERES observed ASR anomalies differences and (bottom) ASR anomalies for ERA-I, for (a),(b) March, (c),(d) April, (e),(f) May, and (g),(h) June.

shortwave radiation entering, and the outgoing short-wave radiation exiting, through the TOA in the spectral range of 0.3 to 5 μm at an accuracy of 5% (Loeb et al. 2009). Monthly averaged CERES EBAF-TOA (Energy Balanced and Filled) edition 2.8 data at spatial resolution of 1° by 1° of incoming and outgoing shortwave radiation are combined to compute the ASR (ASR = SWD$_{TOA}$ − SWU$_{TOA}$) for the Arctic Ocean domain. This domain covers only ocean grids across the entire Arctic Ocean and the seas surrounding the periphery of the Arctic; the domain extent can be seen in Fig. 2.

Shortwave radiation is critically dependent upon the surface albedo and the presence and optical properties of cloud cover. Here, observations of surface albedo from the Climate Monitoring Satellite Application Facility (CM SAF) Cloud, Albedo, and Surface Radiation dataset from AVHRR data, second edition (CLARA-A2; Karlsson et al. 2017) are analyzed. The dataset uses homogenized radiances from passive AVHRR sensors to estimate the monthly averaged terrestrial black-sky surface albedo [see Riihelä et al. (2013) for retrieval details]. Over the polar region, surface albedo measurements are available on an equal-area grid of 25 km^2 from 1982 to 2015; here only the overlap years of 2000–15 are analyzed. Validation over snow and ice surfaces reports that the CLARA-A2 albedo measurements are accurate at typically 3%–15% (Karlsson et al. 2017).

Observations of cloud fraction are analyzed from the Moderate Resolution Imaging Spectroradiometer (MODIS) onboard the *Aqua* satellite since 2002 (King et al. 2003; Platnick et al. 2003). Level-3 monthly averaged cloud fractions from MODIS Collection 6 are available at a global resolution of 1° × 1°, and here they are analyzed from 2003 to 2015. Cloud fraction from the active CALIOP lidar onboard the *CALIPSO* satellite (Winker et al. 2009) is also analyzed for its overlapping data record period of 2007–15. Monthly averaged cloud fraction is obtained from the GCM-Oriented *CALIPSO* Cloud Product (GOCCP) version 2.9 (Cesana and Chepfer 2013). Additionally, a hybrid dataset of cloud water path and surface downwelling radiation observations described by Van Tricht et al. (2016) is analyzed to understand the background Arctic water path state and the associated surface radiative fluxes. This dataset builds from *CloudSat* and *CALIPSO* active profile retrievals of cloud microphysical properties (Stephens et al. 2008), which are then used as input to a radiative transfer model to compute radiative flux profiles and surface values (*CloudSat* 2B-FLXHR-lidar; Henderson et al. 2013). These observed profiles of microphysics and radiative fluxes have been optimized for the high-latitude Arctic region, improving on the phase partitioning between liquid and ice hydrometeors, and ultimately improving the radiative fluxes (Van Tricht et al. 2016). This dataset is only available for 2007–10, and thus is only

used here to characterize the background state of observed cloud water paths and radiation.

An aim of this study is to understand the capacity and potential limitations of the commonly used European Centre for Medium-Range Weather Forecasts (ECMWF) interim reanalysis (ERA-Interim, hereinafter ERA-I; Dee et al. 2011) for applications related to the ASR during spring over the Arctic Ocean domain. As mentioned above, ERA-I has been the trusted dataset by various studies in identifying correlations between springtime radiative flux anomalies and late summer Arctic sea ice extent (Graversen et al. 2011; Kapsch et al. 2013; 2014; Cox et al. 2016; Mortin et al. 2016). Here, 6-h reanalyzed fields on an equal-angle spatial resolution of 0.75° are averaged to monthly mean values. Similar to the state-of-the-art satellite observations, ERA-I variables analyzed include TOA ASR, surface albedo, and cloud fraction. ERA-I sea ice albedo is essentially determined as a time-varying climatological value (ECMWF 2008a) based on bare sea ice and dry snow-covered sea ice albedo values determined by Ebert and Curry (1993); information regarding sea ice concentration is assimilated from passive microwave satellite measurements (ECMWF 2008b). Additionally, surface LWD and SWD from the reanalysis are analyzed in unison with cloud liquid and ice water path values in an effort to characterize the relationship between clouds and downwelling radiative fluxes.

b. Analysis methodology

Introduced in section 1, standardized anomalies of September SIE are computed from the full National Snow and Ice Data Center (NSIDC) observational record during 1979 to 2016. The years are separated into LIYs and HIYs if their 2000 to 2016 September standardized SIE anomaly was greater than ±0.5 (Fig. 1a). For the analyzed span of years, this resulted in 5 years determined as LIY anomalies (2007, 2008, 2010, 2011, and 2012) and 7 as HIY anomalies (2000, 2001, 2003, 2004, 2006, 2013, and 2014). Spring and early summer anomalies of ASR, surface albedo, and cloud fraction for these two groups of years are computed by detrending the 2000 to 2016 record for each month. The analysis then compares monthly composites of detrended anomalies for all LIYs and HIYs for ERA-I reanalysis and the different observations.

3. Results

a. ASR anomalies

Detrended anomaly composite differences (all LIYs − all HIYs) in ASR reveal interesting differences and similarities comparing the CERES observations with ERA-I (Fig. 2). Near the landmasses and around the periphery of the sea ice edge, observations and reanalysis are in agreement regarding positive anomalies (increase) in ASR during March through May of LIYs (Figs. 2a–f). The anomaly differences are smallest in March, increasing in magnitude through the remainder of the spring and early summer months. Differences between observed and reanalysis ASR anomalies emerge in the regional extent and absolute magnitude. Positive ASR anomalies around the Arctic Ocean periphery are generally larger and their spatial extent is greater in the observations compared to ERA-I; this is especially the case around the Eurasian landmass, the western Beaufort Sea, and near the Canadian archipelago (Figs. 2a–f). Likewise, ERA-I captures weak but negative ASR anomalies during LIYs across much of the central Arctic Ocean that are in disagreement with CERES observations during March and April (Figs. 2a–d).

By June, very large differences in ASR anomalies exist between CERES and ERA-I (Figs. 2g,h). Observations show large positive anomalies exceeding $+12\,W\,m^{-2}$ over much of the ocean domain, whereas ERA-I positive ASR anomalies are broadly weaker and lack similar spatial extent; they even indicate a large swath of negative anomalies over the eastern Arctic Ocean. The strength and northward extent of negative ASR anomalies over the Greenland and Barents Seas is also more pronounced in ERA-I relative to CERES.

Monthly-integrated ASR anomalies over the entire Arctic Ocean domain are compared for CERES (full colors) and ERA-I (light colors) in Fig. 3. Observations (black) indicate a steady increase and separability in ASR between LIYs and HIYs through spring and early summer, from $0.25\,W\,m^{-2}$ up to $12\,W\,m^{-2}$ (note ordinate limited to $7\,W\,m^{-2}$). Conversely, the reanalysis only reveals integrated, Arctic-wide positive anomalies in LIY–HIY ASR during April and May (gray), in which the separability of these anomalous LIY and HIY states is a factor of 2 smaller than observed.

Detrended anomalies in ASR for LIYs (reds) and HIYs (blues) are also shown for each month. The LIY anomalies in ASR during April are slightly positive and of similar magnitude in observations and reanalysis. However by May, observations indicate nearly a factor of 2 greater ASR compared to reanalysis. Cumulatively, the observed anomalies in LIY ASR for March through May suggest an additional $2.34\,W\,m^{-2}$ of absorbed shortwave radiation, compared to $1.33\,W\,m^{-2}$ for ERA-I. The positive anomalies in LIY ASR persist into June, where the observed anomaly is $+6.5\,W\,m^{-2}$ while ERA-I is slightly negative.
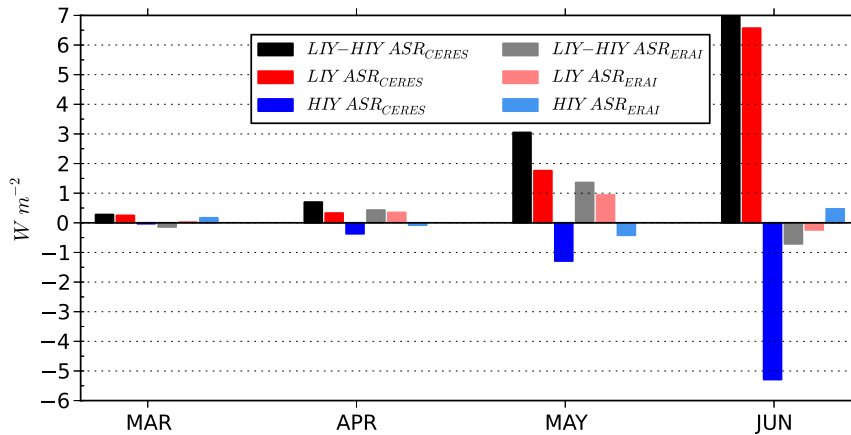
FIG. 3. Monthly Arctic Ocean domain-averaged detrended ASR anomaly differences (LIYs − HIYs) for CERES observations (black) and ERA-I reanalysis (gray). Individual LIY and HIY detrended monthly ASR anomalies for CERES are shown as red and blue bars, respectively; correspondingly, the individual LIY and HIY detrended monthly ASR anomalies in ERA-I are shown as light red and light blue bars, respectively. All values in $W\,m^{-2}$.

Anomaly differences between observations and re-analysis for HIY ASR (Fig. 3, blues) are also intriguing. ERA-I generally fails to capture the extent of increasing negative anomalies in ASR observed by CERES as spring evolves. In fact, ERA-I has slightly positive anomalies in HIY ASR for both March and June. Even when observations and reanalysis agree on negative ASR anomalies during April and May, the magnitude is still underestimated by a factor of 3 to 4. These results suggest that the variability between LIYs and HIYs is systematically underestimated in ERA-I, and thus a robust signal in ASR differences in spring–early summer may be artificially absent in the reanalysis.

b. Year to year variability in radiation for LIYs

The variability between domain-integrated LIY and HIY ASR (Fig. 3) is closely related to the spatial variability and magnitude differences in ASR anomalies between observations and reanalysis shown in Fig. 2. To examine yearly variability, detrended anomalies in ERA-I LWD and SWD radiation for all five April LIYs are shown as an example (Fig. 4). Except for 2008 and 2012, large positive anomalies in LWD were present across a majority of the Arctic Ocean (Fig. 4a). Analogously, the regions with positive (negative) LWD anomalies also reveal distinct negative (positive) SWD anomalies (Fig. 4b). This inverse relationship is consistent with enhanced cloudiness during LIYs, which acts to shield the surface from shortwave radiation and at the same time enhance the longwave reemitted back to the surface. However, the regional extent of the downwelling surface radiation anomalies is not consistent from year to year. This indicates that atmospheric

circulation anomalies, such as enhanced or dampened meridional moisture convergence (Kapsch et al. 2013), are important in determining the location of anomalous fluxes.

Year to year variability in the geographic location and magnitude of ASR anomalies between ERA-I and CERES is even larger. The LIY ASR anomaly differences (ERA-I − CERES) illustrate the regions across the Arctic where the reanalysis is exaggerating (red contours) or under-representing (blue contours) ASR relative to observed (Fig. 4c). It is apparent that deficits in surface SWD are not a prerequisite for a reduction in ASR in the reanalysis. For example, in 2007, 2010, and 2011 the ASR anomaly differences are positive and considerably larger than observed over regions that experienced broad coverage of negative (positive) SWD (LWD) anomalies. Alternatively, during 2008, CERES ASR anomalies were larger than ERA-I across much of the domain. This year-to-year spatial variability results in an April anomaly composite that fails to fully reflect the rather large regional anomaly differences that exist between the observations and reanalysis (Fig. 4c, bottom right).

c. ASR and surface albedo anomalies

In Fig. 5, the April through June evolution of ASR and surface albedo anomaly differences (ERA-I − observations) are shown for the LIYs. Since the amount of ASR at a particular location will be influenced by the local surface albedo, the evolution of ASR and albedo anomalies are examined together.

A weak signal emerges for the LIYs of April (Figs. 5a,b), where the positive anomaly differences in ASR (more anomalous ASR in ERA-I than CERES) (Fig. 5a) tend to
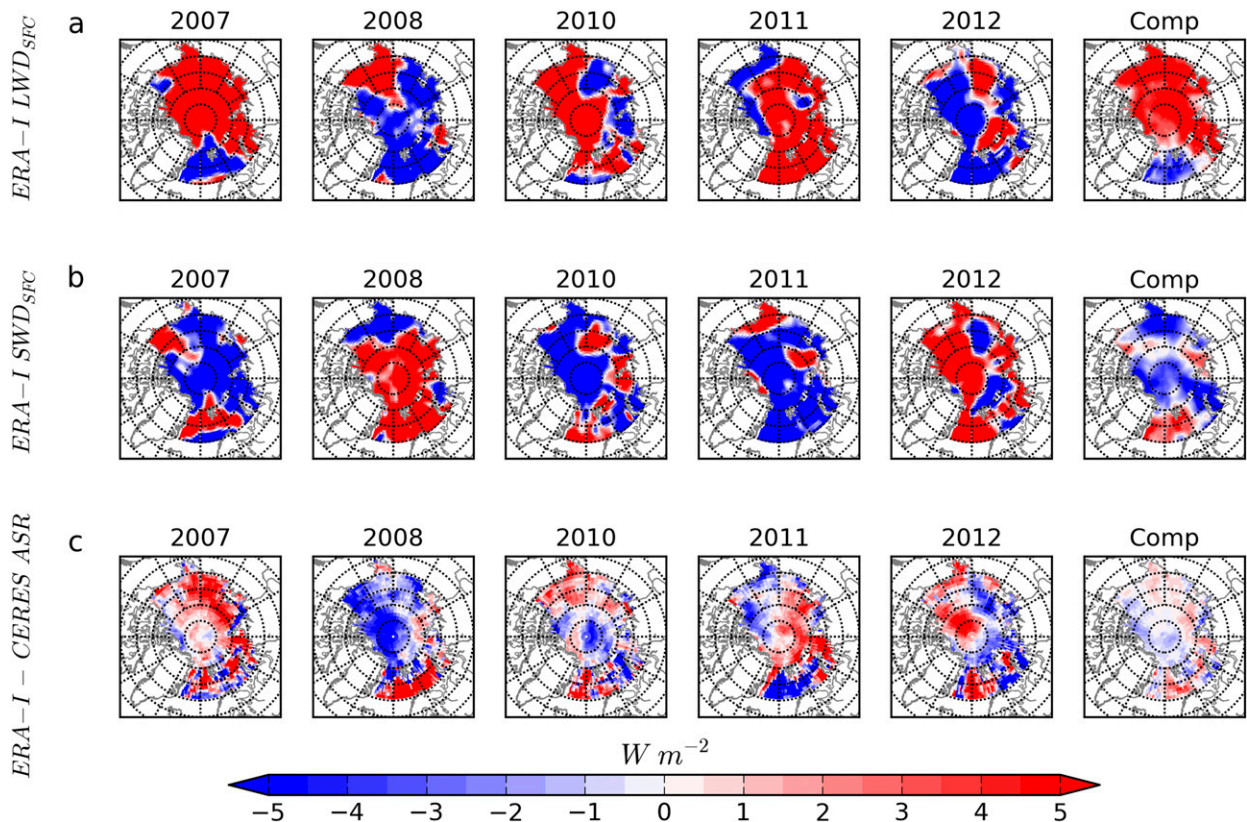
FIG. 4. (a) (left to right) The 2007 to 2012 variability in the April LIY detrended anomalies (W m^{-2}) in ERA-I surface downwelling longwave (LWD) and the composite of all 5 LIYs for April. (b),(c) As in (a), but for the shortwave (SWD) radiation and the detrended anomaly differences in ASR for ERA-I − CERES observations For (c), warmer (cooler) colors indicate that detrended ASR anomalies from ERA-I are overestimated (underestimated) relative to CERES observations.

match with negative anomaly differences in albedo (lower albedo in ERA-I than CLARA-A2) (Fig. 5b). Likewise, regions where the differences in ASR anomalies are negative (more ASR in CERES than ERA-I) are broadly consistent with ERA-I albedo anomalies larger than the observed anomalies. This relationship becomes stronger and more distinct in May (Figs. 5c,d) and June (Figs. 5e,f) when the absolute magnitude of both ASR and albedo anomalies become larger and more disparate between the reanalysis and observations.

Another important signal in the observations, which is not fully present in ERA-I, is the additional ASR that occurs around the periphery of the Eurasian Arctic coastline. Initially in April this signal is weak and varies from year to year (Fig. 5a). However by May, the individual seas bordering the Eurasian continent exhibit relatively large negative ASR anomaly differences (CERES ASR anomalies greater than ERA-I) (Fig. 5c), and these regions coincide with higher (positive) surface albedo anomalies in the reanalysis compared to observations; this trend continues and amplifies across much of the Arctic Ocean domain in June, coincident with

excessively large surface albedo anomalies in ERA-I (Figs. 5e,f). The seas bordering the Eurasian continent are covered by thinner, first year sea ice. Observational trends show that the spatial extent of this first year ice is increasing (Kwok et al. 2009; Comiso 2012). The transmittance of solar radiation through first year sea ice can be up to 3 times larger than multiyear ice, which may be increasing the ocean storage of heat through increased solar absorption (Nicolaus et al. 2012), especially in the presence of surface melt pond formation (Light et al. 2015). Ocean uptake of solar radiation may then be consumed by the ice through basal melt processes (Nicolaus et al. 2012), further exacerbating sea ice melt. Differences in the ASR and albedo anomalies between reanalysis and observations indicate that the amount of solar radiation absorption during spring and early summer, especially across regions susceptible to seasonal ice melt, is likely underestimated in ERA-I. The climatological values of albedo artificially assigned to sea ice coverage in ERA-I are likely inhibiting a feedback between albedo and shortwave radiation variability. Additionally, it is apparent in Fig. 5 that the year to year
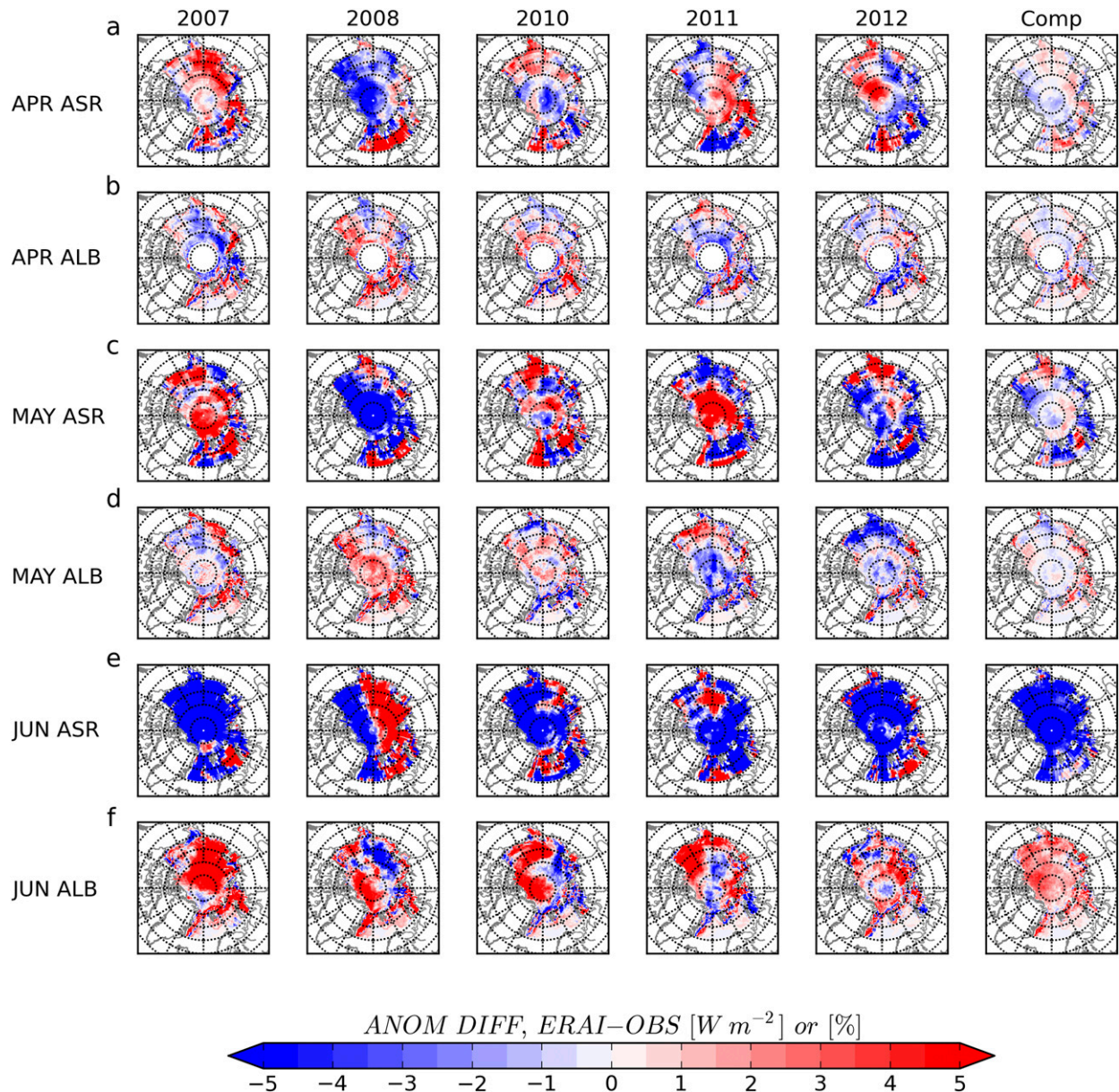
FIG. 5. As in Fig. 4, but for monthly evolution of (a),(c),(e) ASR and (b),(d),(f) surface albedo (ALB) anomaly differences for (a),(b) April, (c),(d) May, and (e),(f) June, respectively, Anomaly differences are defined as ERA-I − observation (OBS). March is excluded from the analysis because the solar zenith angle constraints on the retrieval of CLARA-A2 surface albedo limit data coverage north of 74°N for this month. ASR anomaly differences are in W m^{-2}; ALB anomaly differences are in percent (%).

variability in the anomaly differences is considerably larger than composited anomaly differences (rightmost column), as well as being considerably larger than the LIY − HIY anomaly composites shown in Fig. 2.

d. Observed and reanalysis covariability in ASR and surface albedo

To test how ASR anomalies vary with surface albedo, the covariance and linear regression statistics were computed from the spatially resolved LIY anomalies. The detrended anomalies in ASR and albedo from April through June for each of the five LIYs identified are combined in chronological order, and the covariance and linear regression are then computed. These statistics provide a measure of the relationship between these two variables through the spring months, which is important to assess whether anomalies in a preceding month are preconditioning the anomalies for a subsequent month.
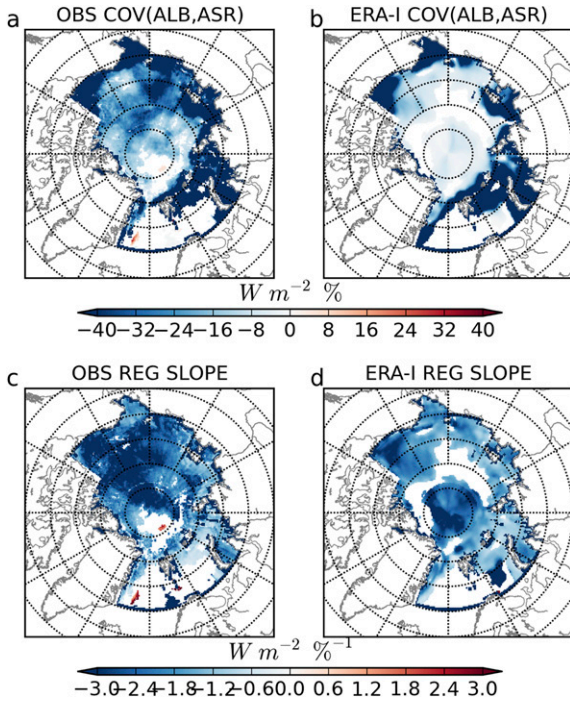
FIG. 6. Spatial distribution of the (a) observed and (b) reanalysis covariance (W m^{-2} %) between detrended anomalies in surface albedo (ALB) and ASR for April through June for all LIYs. (c), (d) The spatial distribution of the linear regression slope (W m^{-2} %$^{-1}$) when detrended anomalies of ASR are regressed onto the detrended anomalies of ALB for April through June for all LIYs. In all panels, data are masked (values = 0) where the correlation of the linear regression between the respective datasets is insignificant ($p > 0.05$).

Covariance between albedo and ASR (Figs. 6a,b) indicates that both observations and reanalysis capture the analog behavior of these anomalies (negative albedo anomalies collocate with positive ASR anomalies in time). Additionally, ERA-I captures the "hotspots" found in the observations of enhanced covariance around the periphery of the Arctic domain. However, they differ in their poleward extent. Negative covariance in the observations extends farther poleward, especially across the Laptev and East Siberian Seas, and north of the Beaufort Sea into the central Arctic. Corresponding linear regression of ASR with surface albedo anomalies (Figs. 6c,d) highlights these same regions where covariance differences are largest between observations and reanalysis. Across much of the Pacific Arctic domain, observed linear regressions are ≥1 W m^{-2} per change in unit albedo (%) compared to ERA-I.

e. Clouds and radiation

An accurate representation of cloud cover will play a crucial role in the radiative energy fluxes. In Fig. 7, active (CALIPSO-GOCCP 2007–15, black) and passive
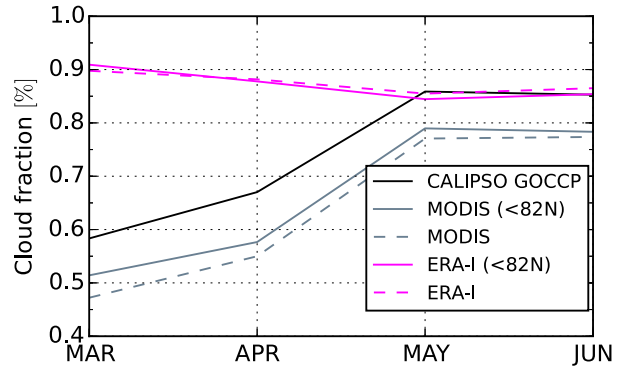

FIG. 7. Monthly averaged Arctic Ocean cloud fraction (%) from CALIPSO GOCCP (black), MODIS (gray), and ERA-I (magenta). Cloud fractions for the domain area coverage of CALIPSO GOCCP (<82°N) for MODIS and ERA-I are shown in solid lines; the full Arctic Ocean domain averages for these datasets are in dashed lines.

(MODIS 2003–15, gray) satellite sensors show a consistent increase in domain-averaged cloud fraction from spring to early summer; the active sensor is very sensitive to cloud hydrometeors and does not rely on solar and infrared signal separability between cloud and surface in its cloud masking like the passive sensor; thus, more clouds are seen by the lidar sensor in the CALIPSO GOCCP record that are artificially designated as clear sky by the passive MODIS sensor. The observations suggest the Arctic region is generally more frequently cloud covered as opposed to cloud free. However ERA-I cloud fractions during spring generally do not fall below 85%. The reanalysis (magenta) clearly overestimates cloud cover during March and April, with even a slight decreasing trend in total cloud fraction through the season. The CALIPSO satellite orbit inhibits observations north of 82°N, so the monthly cloud fractions over the full Arctic Ocean domain from MODIS observations and ERA-I are shown as dashed lines. The differences in the domain coverage yield relatively small cloud fraction differences and their temporal trends are consistent. However MODIS does report slightly lower (2%–4%) cloud fractions when including the Arctic Ocean poleward of 82°N.

Despite the low bias of ~10% for MODIS monthly cloud fraction relative to CALIPSO, its length of data record (here 2003–15) and full Arctic spatial coverage make it useful to study the systematic differences in cloud fraction compared to ERA-I. Cloud fraction detrended anomaly differences for LIYs − HIYs are shown in Figs. 8a–h. It is apparent from comparison that observed and reanalysis cloud fraction anomalies lack consistency in the spatial distribution, as well as the magnitude, of the anomalies. In May and June, MODIS suggests that LIYs are characterized by a lower presence
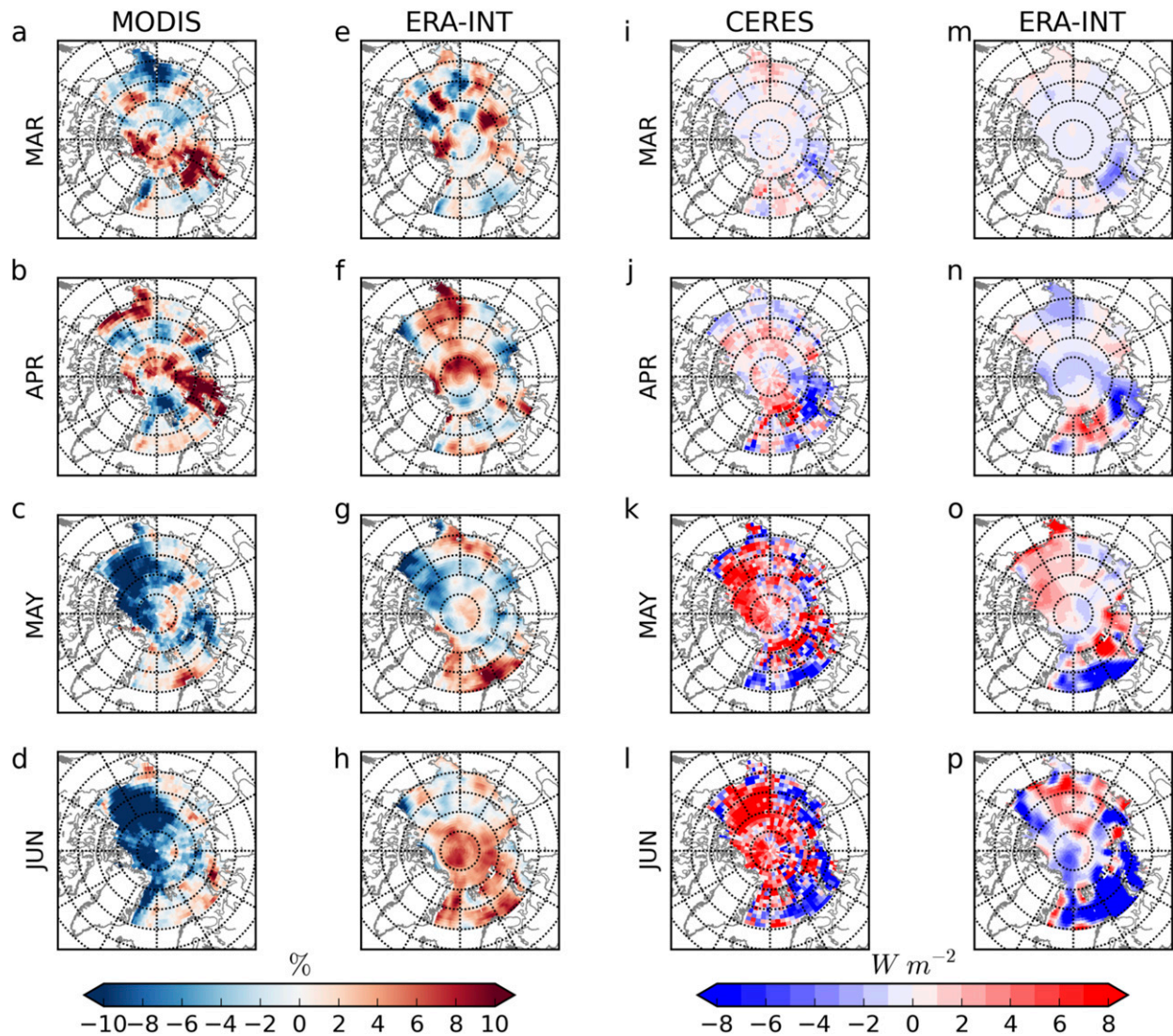
FIG. 8. Detrended cloud fraction anomaly (%) composite differences (LIYs − HIYs) from (a)–(d) MODIS and (e)–(h) ERA-I, and detrended CRE$_{ASR}$ [see Eq. (1)] anomaly (W m^{-2}) composite differences (LIYs − HIYs) for (i)–(l) CERES and (m)–(p) ERA-I. Rows represent each month from top to bottom: March, April, May, and June.

of cloudiness across much of the western Arctic (Figs. 8c,d). ERA-I mimics this cloud reduction in May (Fig. 8g), but by June an opposing increase in cloudiness during LIYs takes over (Fig. 8h).

The radiative impact of these cloud anomalies on ASR can be examined through the cloud radiative effect (CRE) at the TOA. The term CRE$_{ASR}$ [Eq. (1)] is calculated by subtracting the ASR during cloud-free conditions from ASR during all sky conditions:

$$CRE_{ASR} = ASR_{AllSky} - ASR_{ClearSky}. \qquad (1)$$

The spatial distribution of detrended CRE$_{ASR}$ anomalies for LIYs − HIYs are shown in Figs. 8i–p, where

positive anomalies represent increased ASR during LIYs compared to HIYs. It is readily apparent that anomalous CRE$_{ASR}$ corresponds intimately with the location and magnitude of cloud fraction anomalies (Figs. 8a–h). For March and April across much of the central Arctic, relatively weak but positive anomalies in CRE$_{ASR}$ are observed during LIYs, whereas for ERA-I broader coverage of positive cloud fraction anomalies yields weakly negative CRE$_{ASR}$ anomalies. The broad region of increased cloud fraction and reduced CRE$_{ASR}$ for April (Figs. 8f,n) is consistent with the anomalously large (small) surface LWD (SWD) during LIYs shown in Figs. 4a and 4b. By May and June, observed reductions in cloud fraction (Figs. 8c,d) systematically
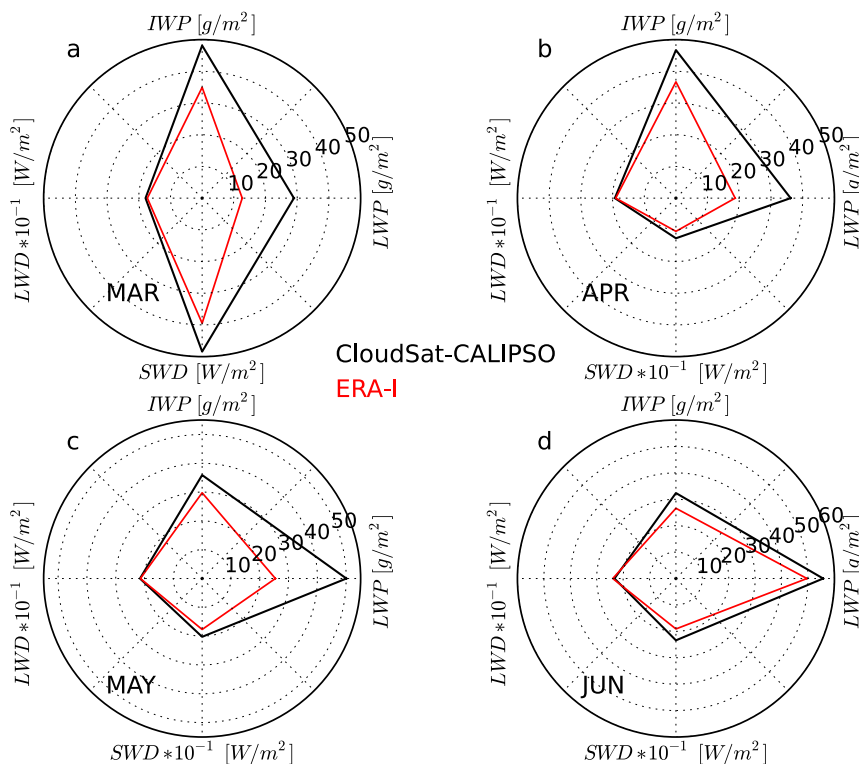
FIG. 9. Polar plot comparison between Arctic Ocean domain-averaged cloud liquid water path [LWP, east $(g\,m^{-2})$], cloud ice water path [IWP, north $(g\,m^{-2})$], surface downwelling longwave [LWD, west $(W\,m^{-2})$] radiation, and surface downwelling shortwave [SWD, south $(W\,m^{-2})$] radiation for *CloudSat–CALIPSO* observations (black; see section 2) and ERA-I (red), for (a) March, (b) April, (c) May, and (d) June. Concentric radial lines represent the water path and surface radiative flux values. Note that all LWD and SWD values [except SWD in (a)] are scaled by a factor 10^{-1} to enable the presentation of all the variables on the same plot.

result in strong, positive anomalies in CRE_{ASR} (Figs. 8k,l); the extent of the reanalysis to capture these anomalies appears to be largely biased in its overrepresentation of cloud, and a general lack of LIY versus HIY variability in cloud fractional anomalies.

f. Cloud microphysics and downwelling surface radiation

Besides total cloud fraction being important for ASR, the microphysical structure of these clouds is also important. Here, Arctic observations of liquid and ice water content profiles are retrieved from a synergy between the radar and lidar instruments onboard *CloudSat* and *CALIPSO* over the period 2007–10. The microphysical profiles are used as input into a radiative transfer model, providing estimates on the downwelling surface radiative fluxes. This dataset has been optimized for Arctic atmospheric conditions (Van Tricht et al. 2016), improving on the retrieved microphysical and radiation profiles of the current version R04 2B-FLXHR-lidar (L'Ecuyer et al. 2008; Henderson et al.

2013). Here, the liquid and ice water content profiles are integrated vertically and provide the total atmospheric column burden of liquid water path (LWP) and ice water path (IWP).

In Fig. 9, observations of Arctic Ocean domain-averaged monthly water paths and surface downwelling radiation (black) are shown together with ERA-I reanalysis averages over the observation period of 2007–10 as a polar plot. Both datasets agree on an increase (decrease) in LWP (IWP) as the season progresses. However, compared to the observations during March through May (Figs. 9a–c), it is apparent that the reanalysis underestimates both the liquid and ice water paths by 10 to $25\,g\,m^{-2}$. The inability to properly partition cloud phase is a general problem with reanalysis and climate models, particularly where cloud liquid condensate is artificially diagnosed as ice (Karlsson and Svensson 2013; Pithan et al. 2014; Sotiropoulou et al. 2016; Lenaerts et al. 2017).

Since the downwelling radiative fluxes at the surface are critically determined by the cloud properties

TABLE 1. Monthly detrended anomalies in ERA-I Arctic Ocean domain-averaged cloud liquid water path (LWP) and surface downwelling longwave (LWD) and shortwave (SWD) radiation for March, April, May, and June. Monthly anomalies are shown LIYs and HIYs (see text).

Month	LWP ($g\,m^{-2}$)		LWD ($W\,m^{-2}$)		SWD ($W\,m^{-2}$)	
	LIY	HIY	LIY	HIY	LIY	HIY
March	0.35	−0.61	1.46	−2.14	−0.31	0.54
April	0.85	−0.49	3.64	−0.70	−1.54	1.16
May	−0.32	−1.01	0.43	−1.21	2.31	−0.30
June	2.78	−1.89	2.44	−2.96	−2.53	2.81

overlying it, the underestimation of cloud water path should therefore impact the surface radiation in opposing ways: a reduction in cloud water 1) should lead to less shortwave reflected to space resulting in overestimated SWD and 2) at the same time should reduce the longwave absorption and reemission to the surface, resulting in underestimated LWD. The average values in Fig. 9 suggest the opposite. Whereas reanalysis and observations agree on the LWD to within a few $W\,m^{-2}$, the reanalysis SWD indicates an increasing negative bias with each passing month, from -10 to $> -40\,W\,m^{-2}$. For March and April, these surface radiation biases are likely a caveat of ERA-I's overabundance of clouds over the Arctic Ocean (Fig. 7), which regardless of their water content would enhance (decrease) the downwelling longwave (shortwave) radiation reaching the surface relative to the observations, indicating more cloud-free sky fraction. For May and June, when average cloud fractional occurrence is similar between observations and reanalysis (Fig. 7), the causes for agreement in LWD and disagreement in SWD are less obvious.

Here, the low bias in ERA-I LWP for all spring months, as well as its potential implications for LWD anomalies during LIYs and HIYs, is examined. Table 1 shows the detrended, domain-averaged LWP, LWD, and SWD anomalies for the spring/early summer months for LIYs and HIYs. Typically LWP anomalies are positive during LIYs, and SWD anomalies follow the trend of increased LWP resulting in more reflective clouds, leading to negative SWD anomalies during LIYs ranging from -0.31 to $-2.53\,W\,m^{-2}$. In terms of LWD, positive anomalies in LWP introduce an increase in the cloud emissivity, which results in positive LWD anomalies that range from 0.43 to $3.64\,W\,m^{-2}$. The sign and magnitude of these LWD anomalies for LIYs agree well with previous studies examining the role of anomalous radiation preconditioning the spring sea ice for subsequent ice melt anomalies through summer (Kapsch et al. 2013; Mortin et al. 2016; Cao et al. 2017).

However, these anomalies in LWP and their impact on cloud emissivity must be put into the context of the background LWP state. Cloud longwave emissivity (ε) is exponentially dependent on the amount of LWP, following the relationship in Stephens (1978):

$$\varepsilon = 1 - e^{(-a \times LWP)}, \qquad (2)$$

where a is the mass absorption coefficient ($-0.158\,m^2\,g^{-1}$; Stephens 1978). The black curve in Fig. 10a shows the exponential increase in emissivity with cloud LWP, which approaches an asymptote near unity (blackbody emitter) near an LWP value of $35\,g\,m^{-2}$ (Stephens 1978; Shupe and Intrieri 2004; Sedlar et al. 2011). Superimposed on Fig. 10a are lines indicating the monthly domain-averaged LWP values from ERA-I for HIYs (dashed) and LIYs (solid), as well as the domain-averaged range of LWP for March through June from *CloudSat–CALIPSO* observations (gray shaded region). The relatively large underestimation of LWP in ERA-I relative to observed LWP range places the cloud emissivity values for ERA-I into a very dynamic emissivity range; the observed range of LWPs instead consist of a sufficient amount of liquid condensate such that emissivity values for all months are generally at or very near a value of unity.

To examine the impact of LWP and potential emissivity biases in ERA-I clouds, fluxes of longwave radiation are estimated using the calculated emissivities from Eq. (2) through the Stefan–Boltzmann relation:

$$LWD = \varepsilon \times \sigma \times T^4, \qquad (3)$$

where σ is the Stefan–Boltzmann constant, and T is the cloud emission temperature. LWD fluxes are calculated using ε computed from the monthly LIY and HIY averaged LWP, across a range of emission temperatures from $-30°$ to $+7°C$. Figure 10b show the anomalies in LWD for LIYs − HIYs. For March and April (magenta and yellow), small changes in LWP ($<2\,g\,m^{-2}$) between LIYs and HIYs cause dramatic changes in ε, resulting in large anomalies in LWD ranging from 12 to over $30\,W\,m^{-2}$ depending on emission temperature. The absolute increase in LWP for both LIYs and HIYs during May (green) reduces the difference in ε and correspondingly the anomalies in LWD are reduced to between 2 and $3\,W\,m^{-2}$. By June (brown), LWPs are well within the blackbody emissivity range, resulting in no difference in corresponding LWD between LIYs and HIYs. The observed range of emissivities generally falls between the estimates for May and June in ERA-I (Fig. 10a, gray shading). This suggests that actual domain-averaged LWD anomalies between LIYs and
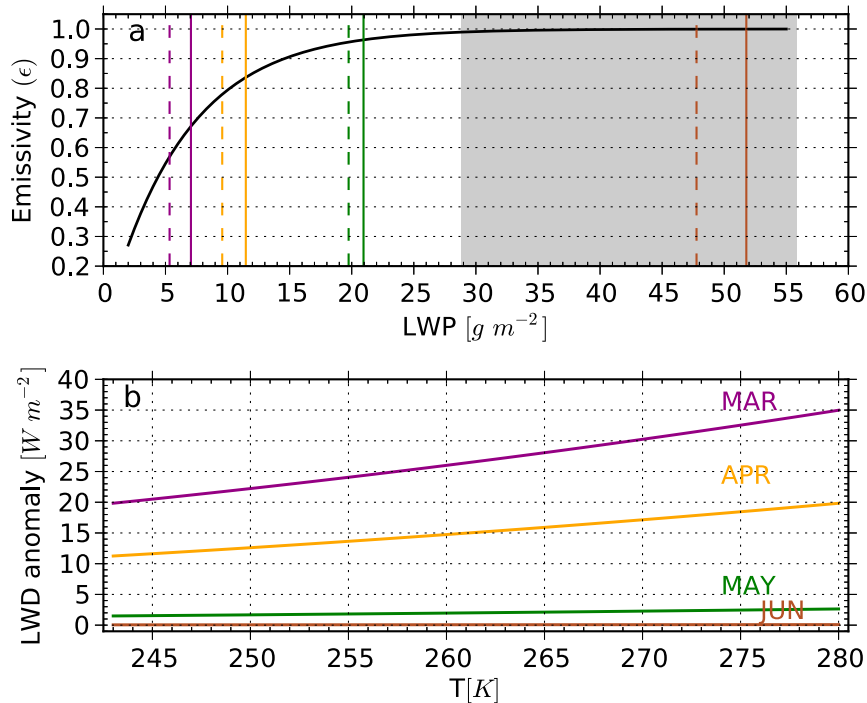
FIG. 10. (a) Theoretical cloud emissivity (ε) as a function of LWP (g m^{-2}) computed from Eq. (2) (black). Vertical lines indicate the HIY (dashed colored lines) and LIY (solid colored lines) domain-averaged LWP values from ERA-I for March (purple), April (yellow), May (green), and June (brown). The corresponding range of LWP for March through June from the *CloudSat–CALIPSO* observations is shaded in gray. (b) ERA-I LWD anomalies [estimated from the Stefan–Boltzmann relationship, Eq. (3), LIY − HIY] emerging due to ε differences for LIYs and HIYs in (a), are shown as a function of emission temperature (K) for each month.

HIYs should lie between the anomalous LWD fluxes estimated for May and June in Fig. 10b. Thus, the overall lack of LWP in ERA-I from March to May leads to an atmospheric state that is overly sensitive to small anomalies in LWP. The anomalies in LWD realized in ERA-I during these months are therefore likely overestimated in the reanalysis.

4. Discussion and conclusions

This paper explores the capacity of the state of the ERA-I reanalysis system relative to state-of-the-art spaceborne observing platforms in representing absorbed shortwave radiation, and the mechanisms that impact shortwave radiation, within the Arctic Ocean climate system during spring. A number of recent studies have identified key anomalies in atmospheric dynamic regimes and radiative fluxes during winter and spring that have been evaluated as critical mechanisms for sea ice preconditioning for the seasonal summer ice melt (Graversen et al. 2011; Sedlar and Devasthale 2012; Kapsch et al. 2013, 2014; Choi et al. 2014; Liu and Key

2014; Mortin et al. 2016; Cao et al. 2017). The majority of these studies have highlighted the role of positive anomalies in downwelling longwave radiation over the sea ice during spring, which effectively limits the amount of sea ice growth during this season, raises surface skin temperatures, and can contribute to earlier onset of ice melt during late spring. Results by Choi et al. (2014), Schröder et al. (2014), and Kashiwase et al. (2017) have found that anomalies in shortwave radiation may also be a critical component of sea ice preconditioning, even during spring and early summer when ice coverage is large and sun angles are low.

Direct observations of ASR from the CERES satellite have revealed that during spring of LIYs, anomalous shortwave radiation is absorbed within the Arctic climate system. Detrended anomalies integrated across the Arctic Ocean domain increase from ~0.3 W m^{-2} in March to ~2 W m^{-2} by May, and during June anomalies surpass 6.5 W m^{-2}. Corresponding LIY ASR anomalies in ERA-I are weaker, being slightly negative during March, increasing through May up to ~1 W m^{-2}, but

being negative again ($-1.5\,\mathrm{W\,m^{-2}}$) in June. Contrasting ASR anomalies between LIYs and HIYs leads to even larger differences, which suggests a systematic shift in spring atmospheric and sea ice properties that modulates the extent, or lack of, shortwave radiation preconditioning. However, in ERA-I the differences in ASR anomalies between LIYs and HIYs are generally weaker, primarily because the variability in processes relevant for ASR anomalies is smaller between the subsets of LIYs and HIYs (see reduced ERA-I HIY ASR anomalies relative to CERES in Fig. 3). A theoretical estimate of the role of anomalous ASR on sea ice thickness changes can be estimated (Thorndike 1992), whereby the domain-averaged monthly anomalous flux difference (LIY − HIY) is multiplied by the latent heat of fusion ($334.4\,\mathrm{kJ\,kg^{-1}}$) and an assumed sea ice density of $917\,\mathrm{kg\,m^{-3}}$. From these estimates, the observed ASR anomalies for March through May can potentially reduce ice thickness by 3.5 cm, compared to 1.4 cm for ERA-I. This thickness change is likely manifested as additional surface melt as the majority of the Arctic is still ice covered in spring. In June alone, the observed anomalous ASR can theoretically add an additional 10 cm of ice melt, compared to −0.6 cm (ice growth) for ERA-I.

While these integrated fluxes and theoretical ice thickness changes appear small, regionally the impact of ASR anomalies during spring is often much larger. It has been shown that the largest differences between observations and reanalysis in ASR tend to occur near the coasts around the eastern Arctic continents and corresponding seas, as well as across the high-latitude central Arctic Ocean ice pack. Significant interannual variability in the ASR anomaly locations is present. This variability can negatively impact the extent of how effective preconditioning can be, since preconditioning is a cumulative concept that is dependent upon the extent and magnitude of anomalous forcing from previous months. Furthermore, this relatively large year-to-year variability is likely to be missed by examining the average, or composite, of HIY or LIY months together (see Fig. 5).

Observations of detrended surface albedo and ASR anomalies tend to show stronger and broader regions of negative covariance within the seas north of the Eurasian continent, and north toward the central Arctic Ocean, compared with ERA-I. Linear regression of ASR with surface albedo further indicates that the covarying anomalies are cumulative from April onward to June, pointing toward a shortwave preconditioning mechanism that is potentially realized during spring. The dominance of negative covariance hotspots observed near the southern edge of the domain is consistent

with the region where Kashiwase et al. (2017) propose that enhanced ice divergence and increased open water fraction may be active; increased shortwave radiation absorption and an enhancement of lateral and basal ice melt may further contribute to shortwave sea ice preconditioning. This process, if active, appears to be mitigated in ERA-I, potentially by biases in the climatological time-variant sea ice albedo, or in the cloud cover variability during the late spring and early summer.

It is evident that longwave radiation from clouds and water vapor is a critical preconditioning mechanism during spring. Anomalies in LWD will modify the sea ice pack, and these modifications can then be acted upon by shortwave radiation. However, these modifications make it difficult to separate preconditioning effects solely due to shortwave radiation, as it becomes more a matter of timing for the respective anomalies (Cox et al. 2016). However, corroborating results from Lenaerts et al. (2017), it was found that ERA-I has a tendency to underestimate the amount of cloud liquid water path, especially during spring (Fig. 10). The lower liquid water paths causes these clouds to exhibit graybody emissivity properties, such that small changes in liquid water path produce large changes in emissivity; the observations during spring were generally within an emissivity range near its asymptote of unity. The large increases in anomalous LWD for relatively small cloud water path increases found in ERA-I are thus likely overestimated. Systematically, the relative strength of monthly LWD anomalies due to clouds in spring for LIYs reported in Kapsch et al. (2013) and Mortin et al. (2016) are likely biased toward the high end.

The observations analyzed in this study indicate that shortwave radiation may be an effective forcing mechanism contributing to springtime preconditioning of Arctic sea ice. While the general signal of shortwave radiation anomalies is broadly consistent in ERA-I, the regional extent and magnitude of this process differ from observations as a result of biases in surface albedo, cloud fraction, and potentially cloud microphysics. As ice extent and volume continue to decrease in the future, the role of ASR during spring may become even more important in preconditioning the ice; potentially further exacerbating seasonal Arctic ice melt.

REFERENCES

Cao, Y., S. Liang, X. Chen, T. He, D. Wang, and X. Cheng, 2017: Enhanced wintertime greenhouse effect reinforcing Arctic amplification and initial sea-ice melting. *Sci. Rep.*, **7**, 8462, https://doi.org/10.1038/s41598-017-08545-2.

Cavalieri, D. J., and C. L. Parkinson, 2012: Arctic sea ice variability and trends, 1979–2010. *Cryosphere*, **6**, 881–889, https://doi.org/10.5194/tc-6-881-2012.

——, ——, P. Gloersen and H J. Zwally, 1996: Sea Ice Concentrations from Nimbus-7 SMMR and DMSP SSM/I-SSMIS Passive Microwave Data, Version 1. NASA National Snow and Ice Data Center Distributed Active Archive Center, Boulder, CO, accessed 23 November 2016, https://doi.org/10.5067/8GQ8LZQVL0VL.

Cesana, G., and H. Chepfer, 2013: Evaluation of the cloud thermodynamic phase in a climate model using CALIPSO-GOCCP. *J. Geophys. Res. Atmos.*, **118**, 7922–7937, https://doi.org/10.1002/jgrd.50376.

Choi, Y.-S., B.-M. Kim, S.-K. Hur, S.-J. Kim, J.-H. Kim, and C.-H. Ho, 2014: Connecting early summer cloud-controlled sunlight and late summer sea ice in the Arctic. *J. Geophys. Res. Atmos.*, **119**, 11 087–11 099, https://doi.org/10.1002/2014JD022013.

Comiso, J. C., 2012: Large decadal decline of the Arctic multiyear ice cover. *J. Climate*, **25**, 1176–1193, https://doi.org/10.1175/JCLI-D-11-00113.1.

Cox, C. J., T. Uttal, C. N. Long, M. D. Shupe, R. S. Stone, and S. Starkweather, 2016: The role of springtime Arctic clouds in determining autumn sea ice extent. *J. Climate*, **29**, 6581–6596, https://doi.org/10.1175/JCLI-D-16-0136.1.

de Boer, G., and Coauthors, 2014: Near-surface meteorology during the Arctic Summer Cloud Ocean Study (ASCOS): Evaluation of reanalyses and global climate models. *Atmos. Chem. Phys.*, **14**, 427–445, https://doi.org/10.5194/acp-14-427-2014.

Dee, D. P., and Coauthors, 2011: The ERA-Interim reanalysis: Configuration and performance of the data analysis system. *Quart. J. Roy. Meteor. Soc.*, **137**, 553–597, https://doi.org/10.1002/qj.828.

Ebert, E. E., and J. A. Curry, 1993: An intermediate one-dimensional thermodynamic sea ice model for investigating ice–atmosphere interactions. *J. Geophys. Res.*, **98**, 10 085–10 109, https://doi.org/10.1029/93JC00656.

ECMWF, 2008a: Part IV: Physical processes. IFS Documentation–CY33R1, European Centre for Medium-Range Weather Forecasts, 162 pp.

——, 2008b: Part II: Data assimilation. IFS Documentation–CY33R1, European Centre for Medium-Range Weather Forecasts, 160 pp.

Graversen, R. G., T. Mauritsen, S. Drijfhout, M. Tjernström, and S. Mårtensson, 2011: Warm winds from the Pacific caused extensive Arctic sea-ice melt in summer 2007. *Climate Dyn.*, **36**, 2103–2112, https://doi.org/10.1007/s00382-010-0809-z.

Henderson, D. S., T. L'Ecuyer, G. Stephens, P. Partain, and M. Sekiguchi, 2013: A multisensor perspective on the radiative impacts of clouds and aerosols. *J. Appl. Meteor. Climatol.*, **52**, 853–871, https://doi.org/10.1175/JAMC-D-12-025.1.

Kapsch, M.-L., R. G. Graversen, and M. Tjernström, 2013: Springtime atmospheric energy transport and the control of Arctic summer sea-ice extent. *Nat. Climate Change*, **3**, 744–748, https://doi.org/10.1038/nclimate1884.

——, ——, T. Economou, and M. Tjernström, 2014: The importance of spring atmospheric conditions for predictions of the Arctic summer sea ice extent. *Geophys. Res. Lett.*, **41**, 5288–5296, https://doi.org/10.1002/2014GL060826.

——, ——, M. Tjernström, and R. Bintanja, 2016: The effect of downwelling longwave and shortwave radiation on Arctic summer sea ice. *J. Climate*, **29**, 1143–1159, https://doi.org/10.1175/JCLI-D-15-0238.1.

Karlsson, J., and G. Svensson, 2013: Consequences of poor representation of Arctic sea-ice albedo and cloud-radiation interactions in the CMIP5 model ensemble. *Geophys. Res. Lett.*, **40**, 4374–4379, https://doi.org/10.1002/grl.50768.

Karlsson, K.-G., and Coauthors, 2017: CLARA-A2: The second edition of the CM SAF cloud and radiation data record from 34 years of global AVHRR data. *Atmos. Chem. Phys.*, **17**, 5809–5828, https://doi.org/10.5194/acp-17-5809-2017.

Kashiwase, H., K. I. Ohshima, S. Nihashi, and H. Eicken, 2017: Evidence for ice-ocean albedo feedback in the Arctic Ocean shifting to a seasonal ice zone. *Nat. Sci. Rep.*, **7**, 8170, https://doi.org/10.1038/s41598-017-08467-z.

King, M. D., and Coauthors, 2003: Cloud and aerosol properties, precipitable water and profiles of temperature and water vapor from MODIS. *IEEE Trans. Geosci. Remote Sens.*, **41**, 442–458, https://doi.org/10.1109/TGRS.2002.808226.

Kwok, R., and D. A. Rothrock, 2009: Decline in Arctic sea ice thickness from submarine and ICESat records: 1958–2008. *Geophys. Res. Lett.*, **36**, L15501, https://doi.org/10.1029/2009GL039035.

——, G. F. Cunningham, M. Wensnahan, I. Rigor, H. J. Zwally, and D. Yi, 2009: Thinning and volume loss of the Arctic Ocean sea ice cover: 2003–2008. *J. Geophys. Res.*, **114**, C07005, https://doi.org/10.1029/2009JC005312.

L'Ecuyer, T. S., N. B. Wood, T. Haladay, G. L. Stephens, and P. W. Stackhouse Jr., 2008: Impact of clouds on atmospheric heating based on the R04 CloudSat fluxes and heating rates data set. *J. Geophys. Res.*, **113**, D00A15, https://doi.org/10.1029/2008JD009951.

Lenaerts, J. T. M., K. Van Tricht, S. Lhermitte, and T. S. L'Ecuyer, 2017: Polar clouds and radiation in satellite observations, reanalyses, and climate models. *Geophys. Res. Lett.*, **44**, 3355–3364, https://doi.org/10.1002/2016GL072242.

Light, B., D. K. Perovich, M. A. Webster, C. Polashenski, and R. Dadic, 2015: Optical properties of melting first-year Arctic sea ice. *J. Geophys. Res. Oceans*, **120**, 7657–7675, https://doi.org/10.1002/2015JC011163.

Liu, Y., and J. R. Key, 2014: Less winter cloud aids summer 2013 Arctic sea ice return from 2012 minimum. *Environ. Res. Lett.*, **9**, 044002, https://doi.org/10.1088/1748-9326/9/4/044002.

Loeb, N. G., B. A. Wielicki, D. R. Doelling, G. L. Smith, D. F. Keyes, S. Kato, N. Manalo-Smith, and T. Wong, 2009: Toward optimal closure of the Earth's top-of-atmosphere radiation budget. *J. Climate*, **22**, 748–766, https://doi.org/10.1175/2008JCLI2637.1.

Mortin, J., G. Svensson, R. G. Graversen, M.-L. Kapsch, J. C. Stroeve, and L. N. Boisvert, 2016: Melt onset over Arctic sea ice controlled by atmospheric moisture transport. *Geophys. Res. Lett.*, **43**, 6636–6642, https://doi.org/10.1002/2016GL069330.

Nicolaus, M., C. Katlein, J. Maslanik, and S. Hendricks, 2012: Changes in Arctic sea ice result in increasing light transmittance and absorption. *Geophys. Res. Lett.*, **39**, L25401, https://doi.org/10.1029/2012GL053738.

Parkinson, C. L., and N. E. DiGirolamo, 2016: New visualizations highlight new information on the contrasting Arctic and Antarctic sea-ice trends since the late 1970s. *Remote Sens. Environ.*, **183**, 198–204, https://doi.org/10.1016/j.rse.2016.05.020.

Persson, P. O. G., 2012: Onset and end of the summer melt season over sea ice: Thermal structure and surface energy perspective from SHEBA. *Climate Dyn.*, **39**, 1349–1371, https://doi.org/10.1007/s00382-011-1196-9.

Petty, A. A., D. Schröder, J. C. Stroeve, T. Markus, J. Miller, N. T. Kurtz, D. L. Feltham, and D. Flocco, 2017: Skillful spring forecasts of September Arctic sea ice extent using passive microwave sea ice observations. *Earth's Future*, **5**, 254–263, https://doi.org/10.1002/2016EF000495.

Pithan, F., and T. Mauritsen, 2014: Arctic amplification dominated by temperature feedbacks in contemporary climate models. *Nat. Geosci.*, **7**, 181–184, https://doi.org/10.1038/ngeo2071.

——, B. Medeiros, and T. Mauritsen, 2014: Mixed-phase clouds cause climate model biases in Arctic wintertime temperature inversions. *Climate Dyn.*, **43**, 289–303, https://doi.org/10.1007/s00382-013-1964-9.

Platnick, S., M. D. King, S. A. Ackerman, W. P. Menzel, B. A. Baum, J. C. Riedi, and R. A. Frey, 2003: The MODIS cloud products: Algorithms and examples from Terra. *IEEE Trans. Geosci. Remote Sens.*, **41**, 459–473, https://doi.org/10.1109/TGRS.2002.808301.

Riihelä, A., T. Manninen, V. Laine, K. Andersson, and F. Kaspar, 2013: CLARA-SAL: A global 28 yr timeseries of Earth's black-sky surface albedo. *Atmos. Chem. Phys.*, **13**, 3743–3762, https://doi.org/10.5194/acp-13-3743-2013.

Schröder, D., D. L. Feltham, D. Flocco, and M. Tsamados, 2014: September Arctic sea-ice minimum predicted by spring meltpond fraction. *Nat. Climate Change*, **4**, 353–357, https://doi.org/10.1038/nclimate2203.

Sedlar, J., and A. Devasthale, 2012: Clear-sky thermodynamic and radiative anomalies over a sea ice sensitive region of the Arctic. *J. Geophys. Res.*, **117**, D19111, https://doi.org/10.1029/2012JD017754.

——, and M. Tjernström, 2017: Clouds, warm air, and a climate cooling signal over the summer Arctic. *Geophys. Res. Lett.*, **44**, 1095–1103, https://doi.org/10.1002/2016GL071959.

——, and Coauthors, 2011: A transitioning Arctic surface energy budget: The impacts of solar zenith angle, surface albedo and cloud radiative forcing. *Climate Dyn.*, **37**, 1643–1660, https://doi.org/10.1007/s00382-010-0937-5.

Serreze, M. C., and J. Stroeve, 2015: Arctic sea ice trends, variability and implications for seasonal ice forecasting. *Philos. Trans. Roy. Soc. London*, **373A**, 20140159, https://doi.org/10.1098/rsta.2014.0159.

Shupe, M. D., and J. M. Intrieri, 2004: Cloud radiative forcing of the Arctic surface: The influence of cloud properties, surface albedo, and solar zenith angle. *J. Climate*, **17**, 616–628, https://doi.org/10.1175/1520-0442(2004)017<0616:CRFOTA>2.0.CO;2.

Sotiropoulou, G., J. Sedlar, R. Forbes, and M. Tjernström, 2016: Summer Arctic clouds in the ECMWF forecast model: An evaluation of cloud parameterization schemes. *Quart. J. Roy. Meteor. Soc.*, **142**, 387–400, https://doi.org/10.1002/qj.2658.

Stephens, G. L., 1978: Radiation profiles in extended water clouds. II: Parameterization schemes. *J. Atmos. Sci.*, **35**, 2123–2132, https://doi.org/10.1175/1520-0469(1978)035<2123:RPIEWC>2.0.CO;2.

——, and Coauthors, 2008: CloudSat mission: Performance and early science after the first year of operation. *J. Geophys. Res.*, **113**, D00A18, https://doi.org/10.1029/2008JD009982.

Thorndike, A. S., 1992: A toy model linking atmospheric thermal radiation and sea ice growth. *J. Geophys. Res.*, **97**, 9401–9410, https://doi.org/10.1029/92JC00695.

Tjernström, M., J. Sedlar, and M. D. Shupe, 2008: How well do regional climate models reproduce radiation and clouds in the Arctic? An evaluation of ARCMIP simulations. *J. Appl. Meteor. Climatol.*, **47**, 2405–2422, https://doi.org/10.1175/2008JAMC1845.1.

Van Tricht, K., and Coauthors, 2016: Clouds enhance Greenland ice sheet meltwater runoff. *Nature Commun.*, **7**, 10266, https://doi.org/10.1038/ncomms10266.

Wesslén, C., M. Tjernström, D. H. Bromwich, G. de Boer, A. M. L. Ekman, L.-S. Bai, and S.-H. Wang, 2014: The Arctic summer atmosphere: An evaluation of reanalyses using ASCOS data. *Atmos. Chem. Phys.*, **14**, 2605–2624, https://doi.org/10.5194/acp-14-2605-2014.

Winker, D. M., M. A. Vaughan, A. Omar, Y. Hu, K. A. Powell, Z. Liu, W. H. Hunt, and S. A. Young, 2009: Overview of the *CALIPSO* mission and CALIOP data processing algorithms. *J. Atmos. Oceanic Technol.*, **26**, 2310–2323, https://doi.org/10.1175/2009JTECHA1281.1.